ADVANCED FUNCTIONAL MATERIALS
www.afm-journal.de

Room-Temperature Tailoring of Vertical ZnO Nanoarchitecture Morphology for Efficient Hybrid Polymer Solar Cells

*Yu-Hsiang Sung, Wen-Pin Liao, Dian-Wei Chen, Chun-Te Wu, Geng-Jia Chang, and Jih-Jen Wu**

A ZnO nanoarchitecture, i.e., ZnO nanosheet (NS) framework, is demonstrated to be a promising electron acceptor and direct electron transport matrix for polymer-inorganic hybrid solar cells. The ZnO NS framework is constructed on nanoneedles/indium tin oxide substrate via a room-temperature chemical bath deposition (RT CBD). The framework morphology can be simply tailored by varying the concentration of precursor solution in the RT CBD. The ZnO nanoarchitecture with an appropriate free space between the NSs is consequently demonstrated to facilitate poly(3-hexylthiophene) (P3HT) infiltration, resulting in superior interface properties, i.e., more efficient charge separation and less charge recombination, in the hybrid. Moreover, apart from the characteristics similar to the ZnO nanorod (NR) array, including vertical feature and single crystalline structure, the ZnO NS framework exhibits a slightly larger absorption edge and a faster electron transport rate. A notable efficiency of 0.88% is therefore attained in the ZnO NS-P3HT hybrid solar cell, which is higher than that of the ZnO NR-P3HT hybrid solar cell.

1. Introduction

Hybrid polymer solar cells composed of heterojunctions of oxide nanocrystals (NCs) and conjugated polymer have attracted great interest due to the good physical and chemical stability as well as the low cost of the metal oxide nanocrystals.[1–6] Similar to organic bulk heterojunction (BHJ) solar cell, insufficient connection between oxide nanocrystals results in that carrier transport in the BHJ of polymer and oxide NCs is limited by the poor electron conducting pathway.[6] Therefore, controlling of the morphology of the donor/acceptor in the hybrid active layer is crucial to overcome the limitation. It has been shown that the charge transport properties can be improved by blending anisotropic nanorods (NRs) instead of nanoparticles (NPs) with polymers because of a better physical connectivity of the acceptors.[2,3] Moreover, in situ synthesis of oxide inside the polymer matrix can also provide a connected oxide domain to improve charge transport in the polymer-oxide BHJ solar cells.[5] However, properly balancing carrier generation and transport by adjusting the morphology remains an issue toward more efficient polymer-inorganic BHJ solar cells.[5]

A polymer photovoltaic device structure consisting of a direct and ordered path for photogenerated electrons to the collecting electrode has been proposed.[7] Oxide nanoarchitectures, such as vertically oriented ZnO nanorod (NR) arrays[8–11] and TiO_2 nanotube (NT) arrays,[12] have been utilized as the electron acceptors to construct a direct electron transport pathway in the hybrid polymer-oxide nanostructure solar cells. The ordered metal oxide nanostructures also offer the potential to improve hole mobility.[6,7] To fabricate such hybrid active layer, the oxide nanoarchitectures are first formed on electrodes followed by infiltration of conjugated polymers into the free spaces of nanoarchitectures. These oxide nanoarchitectures have already been employed to be the anode materials in dye-sensitized solar cells (DSSCs).[13,14] Compared to the conventional TiO_2 NP DSSCs, superior electron transport properties have been demonstrated in the DSSCs with one-dimensional ZnO NR and TiO_2 NT photoanodes.[15] The single-crystalline ZnO NRs provide a nearly trap-free transporting path whereas multiple trapping/detrapping events occur within grain boundaries of the TiO_2 NP anode during electron transport process.[16] In addition to the superior electron transport properties, ZnO NRs attract considerable attention for hybrid polymer-oxide photovoltaic device application because of the low crystallization temperature and anisotropic growth behavior.[9,10] However, insufficient surface area of ZnO NR array is always a concern for its application to solar cells.[9,13] Moreover, polymer infiltration behavior mainly governed by the ZnO NR array morphology also significantly influences the performance of the hybrid solar cell.[9,10] Until now, a maximum efficiency of 0.76% is obtained in the hybrid solar cells based on ZnO NR array and poly(3-hexylthiophene) (P3HT).[11]

In this work, ZnO nanostructured frameworks grown on indium tin oxide (ITO) substrates, which are composed of vertical and single crystalline ZnO nanosheets (NSs) as well

---

Y.-H. Sung, W.-P. Liao, D.-W. Chen,
C.-T. Wu, G.-J. Chang, Prof. J.-J. Wu
Department of Chemical Engineering
National Cheng Kung University
Tainan 701, Taiwan
E-mail: wujj@mail.ncku.edu.tw

DOI: 10.1002/adfm.201200415

as the derived tiny branches, are employed to be the electron acceptor and transport channel in the P3HT hybrid solar cell. The ZnO NSs are developed from nanoneedles via a room-temperature (RT) chemical bath deposition (CBD). The NS morphology can be easily tailored by varying the concentration of precursor solution in the RT CBD. In addition to the characteristics of the vertical feature and single crystalline structure, the ZnO NS framework possesses an appropriate free space facilitating P3HT infiltration, a higher absorption edge and a faster electron transport rate, which is superior to ZnO NR array as the electron acceptor and transport channel in the P3HT hybrid solar cells. A remarkable efficiency of 0.88% is therefore attainable in the ZnO NS-P3HT hybrid solar cell, which is higher than the reported maximum efficiency of 0.76% obtained in the ZnO NR-P3HT solar cells.[11]

2. Results and Discussion

For construction of the NS frameworks, the ZnO nanoneedles/ITO substrate (Figure S1a, Supporting Information) was immersed in a stirred aqueous solution of zinc acetate and NaOH at RT. The limpid solution was obtained by preparing a concentrated aqueous solution of zinc acetate/NaOH and subsequently diluting to a specific volume. For simplicity, the ZnO NS frameworks formed using the RT route with the total precursor solution volumes of 58, 62 and 65 mL are named as NS-58, NS-62 and NS-65, respectively. **Figure 1**a–c show the top-view SEM images of the three NS frameworks. The high-magnification SEM image of NS-62 in Figure 1d reveals that the nanostructural frameworks which are composed of 2D and vertical NSs as well as the derived tiny branches are formed on ITO substrates after the RT growth. The "free space" fractions estimated from the top of the ZnO NS samples in Figure 1a–c are 70.3%, 59.8% and 50.0%, respectively. It indicates that the density of NSs on ITO substrate can be tailored by varying the concentration of precursor solution and are in order of NS-65 > NS-62 > NS-58. When increasing the total volume of precursor solution, i.e., reducing the concentration of precursors, the density of NSs will be increased using the RT CBD route. The lengths of the NSs in the three samples are all ~1 μm as shown in the cross-sectional-view images in Figure 1e and Figure S2a,b (Supporting Information). On the other hand, Figure 1f reveals that the sheet thickness of the nanostructures is ≈15 nm.

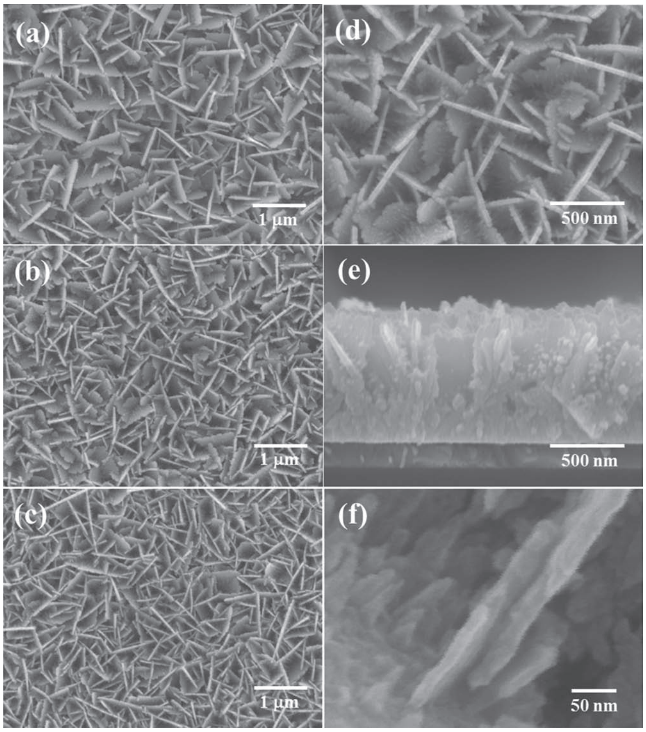

Figure 1. Top-view SEM images of a) NS-58, b) NS-62, and c) NS-65. d) High-magnification top-view and e) cross-sectional-view SEM images of NS-62. f) HR SEM image of NSs.

It is worth addressing here that dimension of the free spaces between the nanoneedles array plays a crucial role for the formation of the NSs. A nanocactus (NC) array instead of the vertical NSs would be formed on the ITO substrate[17] when the density of the one-dimensional nanostructures is higher than ~1×10^8 cm^{-2}. The density of nanoneedle array can be significantly reduced by adding aluminum nitrate into the precursor solution for nanoneedle growth as demonstrated in this work (Figure S1, Supporting Information). Moreover, the 2D NSs are also not attainable if the growth is conducted directly on a seeded ITO substrate in the absence of nanoneedles (Figure S2c, Supporting Information).

X-ray diffraction (XRD) patterns of the three NS samples are shown in Figure S3 (Supporting Information). It reveals that in addition to the diffraction peaks corresponding to ITO substrate, the diffraction peaks of NSs can be indexed as those of ZnO crystal according to ICCD-PDF No. 00-03601451. Moreover, the XRD patterns also demonstrate that the ZnO NSs are preferentially oriented in the [0002] direction. Further structural characterizations of the NSs are carried out by transmission electron microscopy (TEM). We found that the RT-grown nanostructural framework consists of two types of NSs with different exposure surfaces but the same growth direction of [0002] perpendicular to the substrate.

Figure 2a,b show the TEM images of the first type of NS which is developed from the nanoneedles. Figure 2c reveals the high-resolution (HR) TEM image and the corresponding selected area electron diffraction (SAED) pattern (inset) of the region denoted in Figure 2b, which were taken along the zone axis of $[11\bar{2}0]$. They indicate that the NS exhibits a single-crystalline structure of ZnO and the growth directions are along [0002] and $[1\bar{1}00]$. Combining the XRD and TEM results, we conclude that the [0002] and $[1\bar{1}00]$ of ZnO NSs are perpendicular to and parallel to the ITO substrate, respectively. Moreover, the exposure surface of the ZnO NSs developed from nanoneedles is $(11\bar{2}0)$ (a-plan). Figure 2d shows the TEM images of another type of NS which grows alone on the ITO substrate. The HR TEM image and the corresponding SAED pattern taken along the zone axis of $[1\bar{1}00]$ are illustrated in Figure 2e and the inset, respectively. They indicate that the single-crystalline ZnO nanostructure grows along [0002] and $[11\bar{2}0]$ to develop a 2D morphology and the exposure surface of the NS is $(1\bar{1}00)$ (m-plane).

As shown in Figure 1a–c, the dimensions of the ZnO NSs along $[1\bar{1}00]$ and $[11\bar{2}0]$ are always smaller than the thickness of ZnO NSs, indicating the growth rate of the ZnO NS along

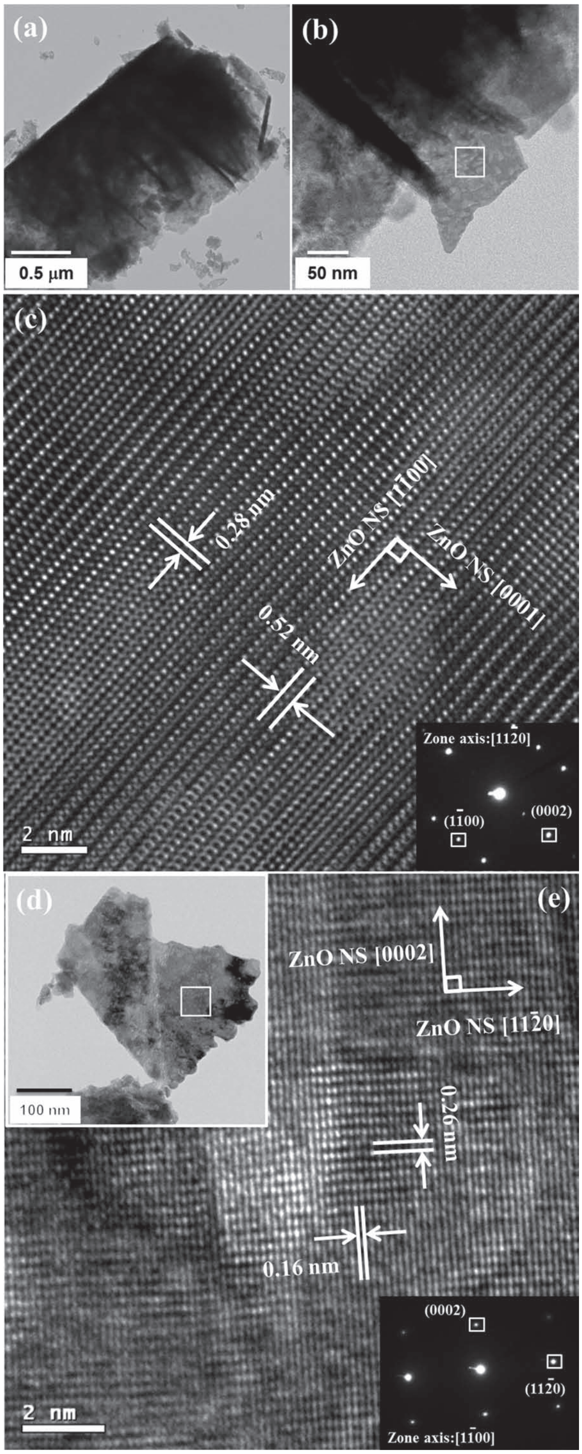

Figure 2. a,b) TEM images of NSs developed from the nanoneedles. c) HRTEM image and the corresponding SAED pattern (inset) of the region denoted in (b). d) TEM images of NS grown on the ITO substrate. e) HRTEM image and the corresponding SAED pattern (inset) of the region denoted in (d).

[0002] is fast than those along the other two directions. With the same growth period, the growth of ZnO NS along [0001] seems not influenced by the concentrations of the precursors, resulting in the same thickness of the three NS samples. However, the relatively slower growth rates of ZnO NS along [1$\bar{1}$00] and [11$\bar{2}$0] are influenced significantly by the concentrations of the precursors. The growth rates along these two directions are decreased by reducing the concentration of precursors, as shown in Figure 1a–c. The result suggests that the growth mechanisms of ZnO NSs along the polar c-plan and nonpolar a-/m-planes may be different by using the RT CBD process.

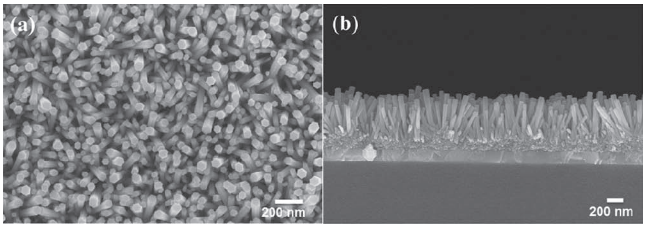

Figure 3. a) Top-view and b) cross-sectional-view SEM images of ZnO NR arrays on ITO substrates.

For comparison, ZnO NR arrays on ITO substrates, as shown in **Figure 3**, were also prepared using CBD method at 95 °C in this work. The density and length of the NR array are 1.7×10^{10} cm^{-2} and 450 nm, respectively. Because the exposure surfaces of the ZnO NR (m-plane)[18] and NS (m- and a- planes) are all nonpolar, the evaluation of relative surface areas of the ZnO NR array and NS-62 was carried out by estimating the amounts of D149 dye adsorption on the two nanostructures (Figure S4, Supporting Information). The result indicates that the surface areas of the two ZnO nanostructures are comparable. Due to the larger length of NSs compared to that of NRs (1 µm vs. 450 nm, as shown in Figure 1e and Figure 3b, respectively), the fact of comparable surface areas of the NS framework and NR array confirms that larger free space exists within the interstices of NS-62 framework. In addition, the absorption spectra of the NS-62 framework and ZnO NR array (Figure S5, Supporting Information) reveal a blue shift of absorption edge of the ZnO NSs compared to that of ZnO NR array. We suggest that the slightly enlarged absorption edge is ascribed to the high nonpolar surface to volume ratio of the NS-62 sample with a sheet thickness of 15 nm.[19]

Figure 4 shows the Raman spectra of P3HT pristine film (on ITO), ZnO NR-P3HT and NS62-P3HT hybrids excited

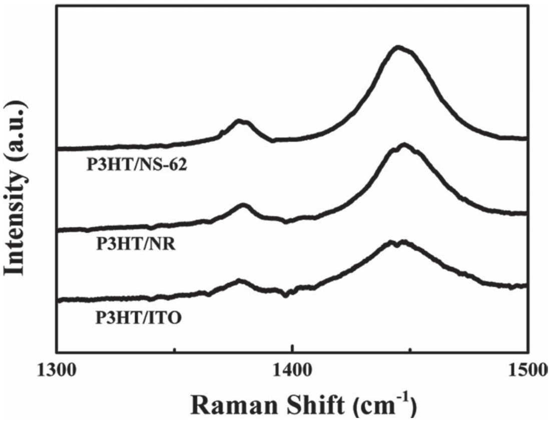

Figure 4. Raman spectra of P3HT pristine film, ZnO NR-P3HT and NS62-P3HT hybrids.

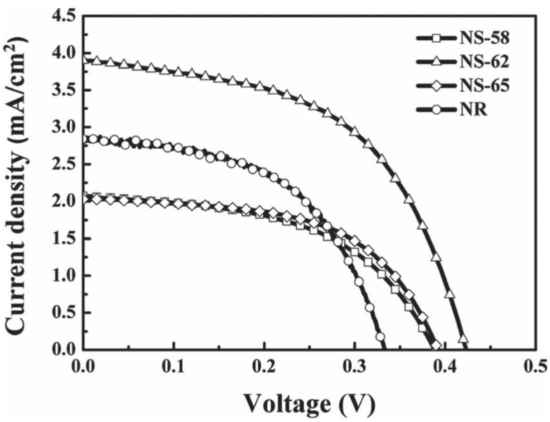

Figure 5. J–V curves of the three ZnO NS-P3HT and ZnO NR-P3HT hybrid solar cells.

at 532 nm. The Raman peaks of the in-plane ring skeleton stretch modes of the thiophene at ~1445–1450 (C=C symmetric stretching) and ~1380 cm^{-1} (C-C intraring stretching)[20] are present in the spectra. It has been reported that the degree of P3HT molecular order can be characterized by the Raman peak position of the symmetric C = C stretch mode.[20,21] The C=C stretch mode of P3HT pristine film is centered at 1445 cm^{-1}, as shown in Figure 4. When P3HT is infiltrated into the ZnO nanostructures, the peak position of the C=C mode of the ZnO NS-P3HT hybrid remains at 1445 cm^{-1} whereas that of the ZnO NR-P3HT hybrid is shifted to 1447 cm^{-1}. A shift in the C=C mode peak position to higher wavenumber indicates the less degree of P3HT molecule order in the ZnO NR-P3HT hybrid.[20,21] On the other hand, better internal order within the P3HT domain, which is comparable with the pristine P3HT, is obtained as P3HT is infiltrated into the ZnO NS framework where larger free space is available compared to ZnO NR array.

The photocurrent density (J)-voltage (V) characteristics of the ZnO NS-P3HT and ZnO NR-P3HT hybrid solar cells are shown in **Figure 5**. The photovoltaic parameters of these hybrid solar cells are summarized in **Table 1**. It reveals that the NR hybrid solar cell fabricated in this work exhibits comparable photovoltaic properties to those reported in literatures.[9] Moreover, the NS-58 hybrid solar cell possesses a slightly higher open circuit voltage (Voc) but a lower short-circuit current density (Jsc) than the NR hybrid solar cell does. As a result, the efficiency of the NS-58 hybrid solar cell is inferior to that of the NR hybrid solar cell. The lower Jsc results from the less interfacial area in the NS-58 hybrid solar cell. The enhanced Voc in the ZnO NS-P3HT hybrid solar cells may be attributed to the slightly larger band gap of NSs than that of NR as shown in Figure S4 (Supporting Information). When increasing the density of ZnO NSs, a Jsc of 3.85 mA/cm^2 is obtained in the NS-62 hybrid solar cell. Compared to the NS-58 hybrid solar cell, an 86% enrichment of the Jsc is achieved by enlarging interfacial area between NSs and P3HT. Voc and fill factor (FF) are also improved in the NS-62 hybrid solar cell as shown in Table 1. A notable efficiency of 0.88% is therefore attained in the ZnO NS-P3HT hybrid solar cell. On the other hand, although the surface areas of ZnO NR array and NS-62 sample are comparable, the NS-62 framework has an advantage over ZnO NR array for P3HT filtration to attain superior interface properties because of its larger free space. The Jsc is therefore enhanced dramatically in the NS-62 hybrid solar cell. Combining with the improved Voc, in this work, a 76% enhancement of the efficiency is demonstrated in the ZnO NS-P3HT hybrid solar cell compared to the ZnO NR-P3HT cell. However, the Jsc and Voc of ZnO NS-P3HT hybrid solar cell decease when the density of NSs is further enhanced, as demonstrated in the NS-65 hybrid solar cell, suggesting that the dimension of free space between NSs is also crucial for P3HT filtration in the ZnO NS-P3HT hybrid solar cells.

Table 1. Photovoltaic properties of the ZnO NS-P3HT and ZnO NR-P3HT hybrid solar cells.

Solar Cell	Voc [V]	Jsc [mAcm^{-2}]	FF	η [%]
NS-65	0.39	2.03	0.56	0.45
NS-62	0.42	3.85	0.54	0.88
NS-58	0.39	2.07	0.51	0.41
NR	0.33	2.84	0.53	0.50

The dynamics of charge separation at the interfaces between the ZnO NSs and P3HT in the hybrids were investigated by TRPL. **Figure 6**a shows the TRPL decay curves of the pristine P3HT and the three ZnO NS-P3HT hybrids on ITO substrates. Because the thickness of the ZnO NR-P3HT hybrid is different from that of the ZnO NS-P3HT one, the TRPL data of ZnO NR-P3HT hybrid is not reported here by considering the PL excitation volume. The instrument response function (IRF, also displayed in Figure 6a) is first eliminated from the decay curves and the decay is subsequently analyzed by biexponential decay kinetics. The average PL lifetimes of the pristine P3HT and the ZnO NS-P3HT hybrids are τ_{P3HT} = 558 ps, $\tau_{\text{NS-65}}$ = 428 ps, $\tau_{\text{NS-62}}$ = 397 ps and $\tau_{\text{NS-58}}$ = 429 ps, respectively. Compared to the pristine P3HT, the reduced PL lifetimes are observed in the ZnO NS-P3HT hybrids. It indicates that charge separation is enhanced as soon as the ZnO NSs are present in the P3HT matrix to provide significantly interfacial areas. Moreover, the NS-62 hybrid has the shortest PL lifetime among the three ZnO NS-P3HT hybrids, revealing that more efficient charge separation occurs in the NS-62 solar cell. It is consistent with the fact that the Jsc of NS-62 solar cell is superior to those of the other two cells. The efficient charge separation in NS-62 hybrid may be ascribed to both appropriate surface area and free space of the ZnO NS framework. The density of NSs in NS-58 is lower than that in NS-62 as shown in Figure 1. It would thus provide a less interfacial area in the NS-58 hybrid solar cell for charge separation. On the other hand, poor P3HT infiltration would take place due to reduction of the free space between NSs when the density of NSs increases further in the NS-65 hybrid. It may influence the interfacial properties between P3HT and ZnO NSs, resulting in that an inferior charge separation and therefore lower Jsc are observed in the NS-65 solar cell compared to the NS-62 solar cell.

Figure 6b displays the dynamics of charge recombination at the interfaces between the ZnO nanostructures and P3HT in the hybrid solar cells, which are determined by EIS

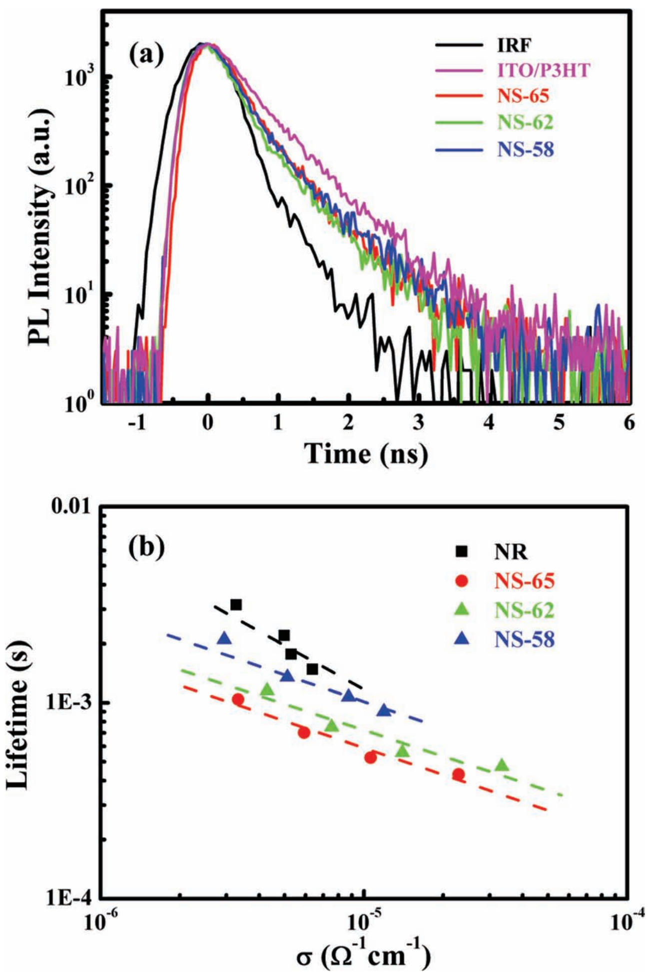

Figure 6. a) TRPL decay curves of the pristine P3HT and the three ZnO NS-P3HT hybrids. b) Electron lifetimes as function of conductivity in the ZnO nanoarchitectures of the P3HT hybrid solar cells.

measurements at Voc. The electron lifetimes in the four ZnO nanostructures are represented as functions of conductivity (σ) in these electron acceptors.[22] It shows that the electron lifetimes in the ZnO NS frameworks of the hybrid solar cells are in order of NS-58 > NS-62 > NS-65 under the same conductivity, i.e. the condition of the conduction bands of ZnO NS frameworks filled with the same amount of photoelectrons.[22] The results indicate that the interfacial recombination increases with the density of ZnO NSs in the ZnO NS-P3HT hybrid solar cell. It may be attributed to the following reasons. First, the less interfacial area in the hybrid solar cell with a low-density NS framework would reduce the probability of interfacial recombination. Moreover, the significant recombination may take place in the hybrid solar cell with a poor interfacial morphology. The interfaces with better compatibility of ZnO NSs and P3HT would be constructed in the hybrid solar cell fabricated using a low-density NS framework, resulting from that the P3HT infiltration can be performed well in the low-density NS framework. When electron lifetimes are compared under the same conductivity of ZnO NSs, as shown in Figure 6b, the influences of bulk defects on the electron lifetime have been ruled out.[22] Once charges separation occurs at interfaces and electrons get into ZnO NSs, the longer electron lifetime would be observed in the hybrid solar cell with less interfacial defects due to good P3HT infiltration.

As shown in Figure 6b, shorter electron lifetimes are observed in the ZnO NS-P3HT hybrid solar cells compared to the ZnO NR-P3HT cell. It may be attributed to relatively larger surface defects formed on the RT-grown NSs compared to the NR array grown at 95 °C. This suggestion is further supported by IMPS measurements, which will be discussed in the next paragraph. In addition, Figure 6b shows that the electron lifetimes in ZnO NR of the hybrid cell are more sensitive to conductivity variation compared to those in the ZnO NSs. Since the conductivity is derived from the transport resistance obtained from EIS measurement, it suggests that the electron transport properties in the two types ZnO nanoarchitectures, i.e., NR array vs. NS framework, are significantly different. Therefore, IMPS was employed to investigate the electron transport behaviors in the ZnO nanoarchitectures of the hybrid solar cells.

Dynamics of electron transport in the hybrid solar cells obtained from IMPS measurements are shown in **Figure 7**. Consistent with the electron transport behavior in the ZnO NW DSSC,[16] the dynamics of electron transport in the ZnO NR-P3HT solar cell are insensitive to light intensity, indicating that very few traps exist in the ZnO NR array. Surprisingly, the electron transit times in the ZnO NS-P3HT hybrid solar cells are significantly shorter than those in the ZnO NR-P3HT cell. By taking the lengths of the nanoarchitectures into account, the electron transport rates are enhanced in the NS-62/P3HT solar cell by factors of 5–12 compared to those in the ZnO NR-P3HT cell as increasing light intensity. On the other hand, the electron transit time in the three ZnO NS-P3HT hybrid solar cells slightly decreases as the light intensity is increased. It is attributed to that more photoelectrons are generated at higher light intensity to fill the deep traps as a result that electron trapping/detrapping involves shallower trap levels only.[23] The light-intensity-depended electron transport behavior indicates that the ZnO NS frameworks possess certain amounts of defects. Nevertheless, the IMPS results demonstrate that ZnO NS-P3HT hybrid solar cells possess superior electron transport properties compared to ZnO NR-P3HT cell. Interestingly, we found that the dynamics of electron transport in the D149-modified ZnO NS-P3HT solar cell are insensitive to light intensity (Figure S6, Supporting Information). It indicates that the defects of ZnO NS frameworks are mainly located on the surfaces of the NSs. The surface defects on the ZnO NS, which can be passivated by dye molecules, intrinsically influence the electron transport properties due to the high surface to volume ratios of the NS nanoarchitectures.

Among the three ZnO NS-P3HT hybrid solar cells, the superior electron lifetime however inferior charge separation are observed in the NS-58 hybrid solar cell. Due to its appropriate NS density, the charge separation in NS-62 hybrid solar cell is improved by the enhanced interfacial area. The efficient charge separation at the interface also suggests a satisfactory interface in the NS-62 hybrid solar cell, which is consistent with the results of EIS measurement. The superior photovoltaic performances are consequently obtained in the NS-62 hybrid solar cell. On the other hand, with the highest NS density, the NS-65 hybrid solar

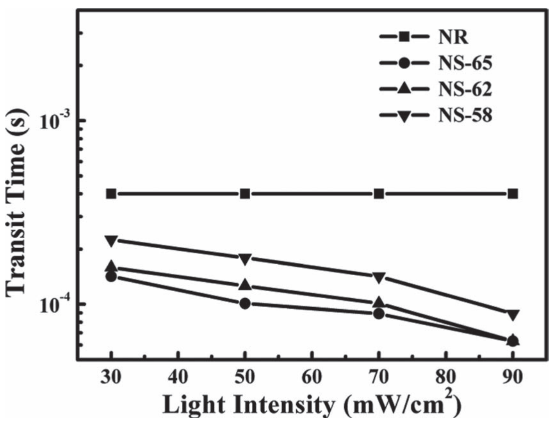

Figure 7. Light intensity dependence of the electron transit times in the ZnO nanoarchitectures of the P3HT hybrid solar cells.

cell possesses both poor charge separation and significant interfacial recombination, resulting in the inferior photovoltaic properties. We therefore conclude that modulation of the NS density in the ZnO NS-P3HT hybrid solar cell, which influences the interfacial area and the dimension of free space between NSs, is very crucial for achieving an efficient hybrid solar cell.

Compared to ZnO NR array, the ZnO NS framework is a superior electron acceptor and transport matrix for hybrid solar cells. In addition to the characteristics of vertical feature and single crystalline structure similar to the ZnO NR, the ZnO NS exhibits a higher absorption edge and a faster electron transport rate due to its high nonpolar surface to volume ratio. Moreover, an appropriate free space within the ZnO NS framework facilitates P3HT infiltration to achieve a superior interface in the ZnO NS-P3HT hybrid. Therefore, in comparison with the ZnO NR-P3HT solar cell in the present work, a 76% enrichment of the efficiency is achieved in the ZnO NS-P3HT hybrid solar cell. Although the larger free space between ZnO NSs facilitates the P3HT infiltration, one may concern the recombination of excitons in infiltrated pure P3HT matrix within ZnO NS framework because of the short exciton diffusion length in P3HT (<10 nm). Since the ZnO NS framework possesses free spaces with a dimension of ~100 nm, we suggest that instead of pure P3HT, various polymer hybrids, such as blended inorganic NP/polymer and in-situ synthesized oxide/polymer, could be also well infiltrated into the ZnO NS framework. Three-dimensional inorganic-polymer hybrid architectures could be constructed for further improvement of the ZnO NS-based hybrid solar cells.

3. Conclusions

The ZnO NS-P3HT hybrid solar cell which possesses superior photovoltaic characteristics to the ZnO NR-P3HT solar cell is demonstrated in this work. The ZnO NS framework composed of vertical and single crystalline ZnO NSs as well as the derived tiny branches are constructed on nanoneedles/ITO substrate via a RT CBD. The NS morphology can be easily tailored by varying the concentration of precursor solution in the RT CBD. In comparison with the ZnO NR array, the ZnO NS framework exhibits a slightly larger absorption edge and fast electron transport properties due to the high nonpolar surface to volume ratio. With a comparable surface area, the ZnO NS framework has an important advantage over the ZnO NR array for P3HT infiltration because of its larger free space between NSs. The results demonstrate that the ZnO NS framework is superior to ZnO NR array as the electron acceptor and transport channel in the P3HT hybrid solar cells. A remarkable efficiency of 0.88% is achieved in the ZnO NS-P3HT hybrid solar cell so far.

4. Experimental Section

To synthesize ZnO NS frameworks, ZnO nanoneedles were first gown on the seeded ITO substrates by CBD at 95 °C for 20 min. The aqueous precursor solution for the ZnO nanoneedles growth consists of zinc acetate (0.02 M) and hexamethylenetetramine (HMTA, 0.02 M), 1,3-diaminopropane (DAP, 190 mM) and aluminum nitrate (6 at%). The seed layer was prepared by the spin coating of a ethanol solution of zinc nitrate and ethanolamine (0.03 M) on the ITO substrate followed by a heat treatment at 350 °C for 1 h. For further construction of the NS frameworks, the ZnO nanoneedles/ITO substrate was immersed in a stirred aqueous solution of zinc acetate and NaOH at RT. The limpid solution was obtained by preparing an aqueous solution (4 mL) of zinc acetate (0.57 M) and NaOH (5 M) and subsequently diluting to a specific volume. For simplicity, the ZnO NS frameworks formed using the RT route with the total precursor solution volumes of 58, 62 and 65 mL are named as NS-58, NS-62 and NS-65, respectively.

The ZnO NR arrays were grown on the seeded ITO substrate by CBD in an aqueous solution of zinc acetate and HMTA (0.03 M) at 95 °C for 30 min. The seeded layers which also perform as the hole blocking layers were deposited on ITO by spin coating method using sol-gel solutions.[24] The precursor solutions were prepared by dissolving zinc acetate and ethanolamine in ethanol with various concentrations. Multiple spin coatings of the ZnO layers were carried out on ITO substrate with the concentration order of precursor solutions being 0.01 M, 0.05 M, 0.1 M, 0.25 M and 0.5 M followed by a heat treatment at 350 °C for 30 min.

The morphologies of the nanoarchitectures were examined using scanning electron microscopy (SEM, JEOL JSM-7000F). The "free space" fractions of the ZnO NS samples are estimated using the software of Sigma Scan Pro. The crystal structures were investigated using XRD (Rigaku D/MAX-2000) and transmission electron microscopy (TEM, FEI E.O Tecnai F20 G2 MAT S-TWIN). Optical absorptions of the ZnO nanoarchitectures were measured using a UV-vis-IR spectrophotometer (JASCO V-670).

ZnO NS-P3HT and ZnO NR-P3HT hybrid solar cells with island-type electrodes[25] were fabricated in this work. P3HT infiltration into the ZnO nanoarchitectures was carried out in a glovebox. The ZnO nanoarchitectures was first wetted with p-xylene and was subsequently covered with a chlorobenzene solution of P3HT (Sigma-Aldrich, Mw = 80 000, 45 mg mL^{-1}). After stilling for 2 min for P3HT infiltrating into the free space of the nanoarchitecture, the sample was then spun to form a thin layer of P3HT on the ZnO-P3HT hybrid. A heat treatment was immediately performed at 150 °C for 20 min. A thin layer of PEDOT:PSS (Baytron PVP AI 4083) was further spun on the ZnO-P3HT hybrid in the air followed by heat treatments at 120 °C and 150 °C for 6 min and 3 min, respectively. Finally, a 100 nm-thick gold film was deposited on the top of PEDOT:PSS layer. A black-painted mask on the ITO substrate side was used to create an exposed area of 0.04 cm^2 for all hybrid solar cells. The degree of P3HT molecular order in the ZnO nanoarchitecture-P3HT hybrids were characterized by Raman spectroscopy (Jobin Yvon/Labram HR) at an excitation length of 532 nm.

Photovoltaic characteristics of the hybrid solar cells were measured under AM-1.5 simulated sunlight at 100 mW cm^{-2} (300 W, Model 91160A, Oriel). Time-resolved photoluminescence (TRPL) spectroscopy measurements were performed using a pulse laser (375 nm) with a pulse width of 70 ps for excitation. The TRPL decays at 650 nm were recorded by a time correlated single photon counting (TCSPC) spectrometer. Electrochemical impedance spectroscopy (EIS) measurements were carried out under the illumination of a green LED light (530 nm) with various intensities by applying a 10 mV ac signal over the frequency range 1–10^5 Hz at the Voc of the hybrid solar cells using a potentiostat with a frequency response analyzer (FRA, Zaher, IM6ex). Two-channel transmission line model was employed to investigate the electron transport and recombination in the hybrid solar cells.[22] Intensity modulated photocurrent spectroscopy (IMPS) measurements were conducted under a modulated green LED light (530 nm) driven by a source supply (Zahner, PP210) and a potentiostat with a FRA (Zaher, IM6ex). The light intensity modulation was 20% of the base light intensity over the frequency range of 1–10^4 Hz. The illumination intensity is variable in the range of 30-90 mWcm^{-2}. The method for extraction of electron transit times in the hybrid solar cells from the IMPS responses has been described in detail elsewhere.[16]

Supporting Information

Supporting Information is available from the Wiley Online Library or from the author.

Acknowledgements

The authors thank Dr. Ching-Hsiang Chen for his technical support on TRPL. Financial supports from the National Science Council in Taiwan under Contract No. NSC 99-2221-E-006-198-MY3 and NSC 100-2628-E006-032-MY2 are gratefully acknowledged.

Received: February 10, 2012
Revised: April 4, 2012
Published online: May 25, 2012

---

[1] C. Y. Kwong, W. C. H. Choy, A. B. Djurisic, P. C. Chui, K. W. Cheng, W. K. Chan, *Nanotechnology* **2004**, *15*, 1156.
[2] Y.-Y. Lin, T.-H. Chu, S.-S. Li, C.-H. Chuang, C.-H. Chang, W.-F. Su, C.-P. Chang, M.-W. Chu, C.-W. J. Chen, *J. Am. Chem. Soc.* **2009**, *131*, 3644.
[3] S.-S. Li, C.-P. Chang, C.-C. Lin, Y.-Y. Lin, C.-H. Chang, J.-R. Yang, M.-W. Chu, C.-W. Chen, *J. Am. Chem. Soc.* **2011**, *131*, 11614.
[4] W. J. E. Beek, M. M. Wienk, R. A. J. Janssen, *Adv. Mater.* **2004**, *16*, 1009.
[5] S. D. Oosterhout, M. M. Wienk, S. S. van Bavel, R. Thiedmann, L. J. A. Koster, J. Gilot, J. Loos, V. Schmidt, R. A. J. Janssen, *Nat. Mater.* **2009**, *8*, 818.
[6] J. Weickert, R. B. Dunbar, H. C. Hesse, W. Wiedemann, L. Schmidt-Mende, *Adv. Mater.* **2011**, *23*, 1810.
[7] A. C. Mayer, S. R. Scully, B. E. Hardin, M. W. Rowell, M. D. McGehee, *Mater. Today* **2007**, *10*, 28.
[8] D. C. Olson, J. Piris, R. T. Collins, S. E. Shaheen, D. S. Ginley, *Thin Solid Films* **2006**, *496*, 26.
[9] Y.-Y. Lin, C.-W. Chen, T.-H. Chu, W.-F. Su, C.-C. Lin, C.-H. Ku, J.-J. Wu, C.-H. Chen, *J. Mater. Chem.* **2007**, *17*, 4571.
[10] Y.-J. Lee, M. T. Lloyd, D. C. Olson, R. K. Grubbs, P. Lu, R. J. Davis, J. A. Voigt, J. W. P. Hsu, *J. Phys. Chem. C* **2009**, *113*, 15778.
[11] L. Baeten, B. Conings, H.-G. Boyen, J. D'Haen, A. Hardy, M. D'Olieslaeger, J. V. Manca, M. K. Van Bael, *Adv. Mater.* **2011**, *23*, 2802.
[12] G. K. Mor, S. Kim, M. Paulose, O. K. Varghese, K. Shankar, J. Basham, C. A. Grimes, *Nano Lett.* **2009**, *12*, 4250.
[13] M. Law, L. E. Greene, J. C. Johnson, R. Saykally, P. D. Yang, *Nat. Mater.* **2005**, *4*, 455.
[14] G. K. Mor, K. Shankar, M. Paulose, O. K. Varghese, C. A. Grimes, *Nano Lett.* **2006**, *6*, 215.
[15] K. Yu, J. Chen, *Nanoscale Res. Lett.* **2009**, *4*, 1.
[16] D. K.-P. Wong, C.-H. Ku, Y.-R. Chen, G.-R. Chen, J.-J. Wu, *ChemPhysChem* **2009**, *10*, 2698.
[17] C.-T. Wu, J.-J. Wu, *J. Mater. Chem.* **2011**, *21*, 13605.
[18] J.-J. Wu, G.-R. Chen, H.-H. Yang, C.-H. Ku, J.-R. Lai, *Appl. Phys. Lett.* **2007**, *90*, 213109.
[19] C.-W. Chen, K.-H. Chen, C.-H. Shen, A. Ganguly, L.-C. Chen, J.-J. Wu, H.-I. Wen, W.-F. Pong, *Appl. Phys. Lett.* **2006**, *88*, 241905.
[20] W. C. Tsoi, D. T. James, J. S. Kim, P. G. Nicholson, C. E. Murphy, D. D. C. Bradley, J. Nelson, J.-S. Kim, *J. Am. Chem. Soc.* **2011**, *133*, 9834.
[21] J.-J. Yun, J. Peet, N.-S. Cho, G. C. Bazan, S. J. Lee, M. Moskovits, *Appl. Phys. Lett.* **2008**, *92*, 251912.
[22] F. Fabregat-Santiago, J. Bisquert, L. Cevey, P. Chen, M. Wang, S. M. Zakeeruddin, M. Gratzel, *J. Am. Chem. Soc.* **2009**, *131*, 558.
[23] T. Oekermann, T. Yoshida, H. Minoura, K. G. U. Wijayantha, L. M. Peter, *J. Phys. Chem. B* **2004**, *108*, 8364.
[24] C.-S. Li, Y.-N. Li, Y.-L. Wu, B.-S. Ong, R.-O. Loutfy, *J. Mater. Chem.* **2009**, *19*, 1626.
[25] M.-S. Kim, M.-G. Kang, L. J. Guo, J. Kim, *Appl. Phys. Lett.* **2008**, *92*, 133301.